POSE MODULATED AVATARS FROM VIDEO

Chunjin Song[1], **Bastian Wandt**[2] **& Helge Rhodin**[1]
[1]Department of Computer Science, University of British Columbia
{chunjins,rhodin}@cs.ubc.ca
[2]Department of Electrical Engineer, Linköping University
bastian.wandt@liu.se

ABSTRACT

It is now possible to reconstruct dynamic human motion and shape from a sparse set of cameras using Neural Radiance Fields (NeRF) driven by an underlying skeleton. However, a challenge remains to model the deformation of cloth and skin in relation to skeleton pose. Unlike existing avatar models that are learned implicitly or rely on a proxy surface, our approach is motivated by the observation that different poses necessitate unique frequency assignments. Neglecting this distinction yields noisy artifacts in smooth areas or blurs fine-grained texture and shape details in sharp regions. We develop a two-branch neural network that is adaptive and explicit in the frequency domain. The first branch is a graph neural network that models correlations among body parts locally, taking skeleton pose as input. The second branch combines these correlation features to a set of global frequencies and then modulates the feature encoding. Our experiments demonstrate that our network outperforms state-of-the-art methods in terms of preserving details and generalization capabilities. Our code is available at https://github.com/ChunjinSong/PM-Avatars.

1 INTRODUCTION

Human avatar modeling has garnered significant attention as enabling 3D telepresence and digitization with applications ranging from computer graphics (Wu et al., 2019; Bagautdinov et al., 2021; Peng et al., 2021a; Lombardi et al., 2021) to medical diagnosis (Hu et al., 2022). To tackle this challenge, the majority of approaches start from a skeleton structure that rigs a surface mesh equipped with a neural texture (Bagautdinov et al., 2021; Liu et al., 2021) or learnable vertex features (Kwon et al., 2021; Peng et al., 2021a;b). Although this enables reconstructing intricate details with high precision (Liu et al., 2021; Thies et al., 2019) in controlled conditions, artifacts remain when learning the pose-dependent deformation from sparse examples. To counteract, existing methods typically rely on a parametric template obtained from a large number of laser scans, which still limits the variety of the human shape and pose. Moreover, their explicit notion of vertices and faces is difficult to optimize and can easily lead to foldovers and artifacts from other degenerate configurations. Moreover, the processed meshes are usually sampled uniformly in one static pose thus not being adaptive to dynamic shape details like wrinkles.

Our objective is to directly reconstruct human models with intricate and dynamic details from given video sequences with a learned neural radiance field (NeRF) model (Mildenhall et al., 2020). Most related are surface-free approaches such as A-NeRF (Su et al., 2021) and NARF (Noguchi et al., 2021) that directly transform the input query points into relative coordinates of skeletal joints and then predict density and color for volumetric rendering without an intermediate surface representation. To further enhance the ability to synthesize fine details, (Su et al., 2022; Li et al., 2023) explicitly decompose features into local part encodings before aggregating them to the final color. Closely related are also methods that learn a neural radiance field of the person in a canonical T-pose (Jiang et al., 2022; Li et al., 2022a; Wang et al., 2022). Despite their empirical success, as depicted in Fig. 1, it is evident that a single query point, when considered in different pose contexts, is difficult to be learned. Specifically, the T-shirt region appears flat in one pose (2nd row) but transforms into a highly textured surface in another (1st row). The commonly used positional encoding (Mildenhall et al., 2020) maps points with fixed frequency transformations and is hence

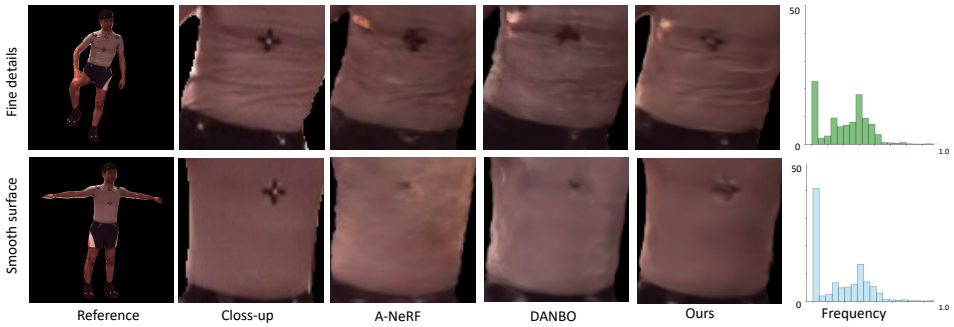

Figure 1: **Motivation.** Our frequency modulation approach enables pose-dependent detail by using explicit frequencies that depend on the pose context, varying over frames and across subjects. Our mapping mitigates artifacts in smooth regions as well as synthesizes fine geometric details faithfully, e.g., when wrinkles are present (1st row). By contrast, existing surface-free representations struggle either with fine details (e.g. marker) or introduce noise artifacts in uniform regions (e.g. the black clouds, 2nd row). To quantify the difference in frequency of these cases, we calculate the standard deviation (STD) pixels within 5×5 patches of the input closeup and illustrate the frequency histograms of the reference. Even for the same subject in similar pose the frequency distributions are distinct, motivating our pose-dependent frequency formulation.

non-adaptive. Entirely implicit mappings from observation to canonical space are complex and contain ill-posed one to many settings. Thus they struggle to explicitly correlate pose context with the matching feature frequency bands of query points. As a result, these methods either yield overly smoothed details or introduce noisy artifacts in smooth regions.

In this paper, we investigate new ways of mapping the skeleton input to frequencies of a dynamic NeRF model to tackle the aforementioned challenges. Specifically, we design a network with a branch that is explicit in the frequency space and build a multi-level representation that adapts to pose dependencies. To accomplish this, we utilize Sine functions as activations, leveraging its explicit notion of frequency and its capability to directly enforce high-frequency feature transformations (Sitzmann et al., 2020; Mehta et al., 2021; Wu et al., 2023). The main challenge that we address here is on how to control the frequency of the Sine activation for deforming characters.

We first apply a graph neural network (GNN) (Su et al., 2022) on the input pose to extract correlations between skeleton joints, thereby encoding pose context. Given query point coordinates for NeRF rendering, the joint-specific correlation features are first combined with a part-level feature aggregation function and then utilized to generate point-dependent frequency transformation coefficients. The frequency modulation process takes place within a set of intermediate latent features, allowing us to optimize the modulation effects at different scales effectively. Lastly, similar to existing NeRF methods, we output density and color to synthesize and render images. Across various scenarios, we consistently outperform state-of-the-art methods. Our core contributions are

- We introduce a novel and efficient neural network with two branches, tailored to generate high-fidelity functional neural representations of human videos via frequency modulation.
- A simple part feature aggregation function that enables high-frequency detail synthesis in sharp regions and reduces artifacts near overlapping joints.
- We conduct thorough evaluation and ablation studies, which delve into the importance of window functions and frequency modulations with state-of-the-art results.

2 Related Work

Our work is in line with those that apply neural fields to model human avatar representations. Here we survey relevant approaches on neural field (Xie et al., 2022) and discuss the most related neural avatar modeling approaches.

Neural Fields. As a successful application, a breakthrough was brought by Neural Radiance Fields (NeRF) (Mildenhall et al., 2020). Recently, extending NeRF to dynamic scenes becomes more and more popular and enables numerous downstream applications (Park et al., 2021a; Pumarola et al., 2021; Park et al., 2021b; Cao & Johnson, 2023). The key idea is to either extend NeRF with an additional time dimension (T-NeRF) and additional latent code (Gao et al., 2021; Li et al., 2022b; 2021b), or to employ individual multi-layer perceptrons (MLPs) to represent a time-varying deformation field and a static canonical field that represents shape details (Du et al., 2021; Park et al., 2021a;b; Tretschk et al., 2021; Yuan et al., 2021). However, these general extensions from static to dynamic scenes only apply to small deformations and do not generalize to novel input poses.

Our method is also related to applying periodic functions for high frequency detail modeling within the context of neural fields. NeRF (Mildenhall et al., 2020) encodes the 3D positions into a high-dimensional latent space using a sequence of fixed periodic functions. Later on, Tancik*et al*. (Tancik et al., 2020) carefully learn the frequency coefficients of these periodic functions, but they are still shared for the entire scene. In parallel, Sitzmann*et al*. (Sitzmann et al., 2020) directly uses a Sine-function as the activation function for latent features, which makes frequency bands adaptive to the input. (Lindell et al., 2022; Fathony et al., 2021) further incorporate the multi-scale strategy of spectral domains to further advance the modeling of band-limited signals. Recently, (Hertz et al., 2021; Mehta et al., 2021; Wu et al., 2023) propose to modulate frequency features based on spatial patterns for better detail reconstructions. However, differing from these methods, we explicitly associate the desired frequency transformation coefficients with pose context, tailored to the dynamics in human avatar modeling.

Neural Fields for Avatar Modeling. Using neural networks to model human avatars (Loper et al., 2015) is a widely explored problem (Deng et al., 2020; Saito et al., 2021; Chen et al., 2021). However, learning personalized body models given only videos of a single avatar is particularly challenging which is our research scope in this paper.

In the pursuit of textured avatar modeling, the parametric SMPL body model is a common basis. For instance, (Zheng et al., 2022; 2023) propose partitioning avatar representations into local radiance fields attached to sampled SMPL nodes and learning the mapping from SMPL pose vectors to varying details of human appearance. On the other hand, approaches without a surface prior, such as A-NeRF (Su et al., 2021) and NARF (Noguchi et al., 2021), directly transform the input query points into relative coordinates of skeletal joints. Later on, TAVA (Li et al., 2022a) jointly models non-rigid warping fields and shading effects conditioned on pose vectors. ARAH (Wang et al., 2022) explores ray intersection on a NeRF body model initialized using a pre-trained hypernetwork. DANBO (Su et al., 2022) applies a graph neural network to extract part features and decompose an independent part feature space for a scalable and customizable model. To reconstruct high-frequency details, Neural Actor (Liu et al., 2021) utilizes an image-to-image translation network to learn texture mapping, with a constraint on performers wearing tight clothes for topological consistency. Further studies (Peng et al., 2021b;a; Dong et al., 2022) suggest assigning a global latent code for each training frame to compensate for dynamic appearance. Most recently, HumanNeRF (Weng et al., 2022) and its following works like Vid2Avatar (Guo et al., 2023) and MonoHuman (Yu et al., 2023) show high-fidelity avatar representations for realistic inverse rendering from a monocular video. Despite the significant progress, none of them explicitly associate the pose context with frequency modeling, which we show is crucial for increasing shape and texture detail.

3 METHOD

Our objective is to reconstruct a 3D animatable avatar by leveraging a collection of N images, along with the corresponding body pose represented as the sequence of joint angles $[\theta_k]_{k=1}^{N}$. Our key technical ingredient is a pose-guided frequency modulation network and its integration for avatar reconstruction. Fig. 2 provides a method overview with three main components. First, we employ a Graph Neural Network (GNN) to estimate local relationships between different body parts. The GNN facilitates effective feature aggregation across body parts, enabling to learn the nearby pose contexts without relying on surface priors. Then the aggregated GNN features are learned to modulate the frequencies of input positions. Lastly, the resulting per-query feature vector is mapped to the corresponding density and radiance at that location as in the original NeRF framework.

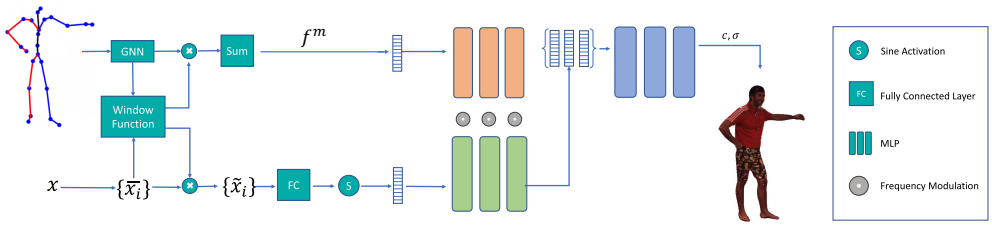

Figure 2: **Method overview.** First, a graph neural network takes a skeleton pose as input to encode correlations of joints. Together with the relative coordinates $\{\bar{x}_i\}$ of query point x, a window function is learned to aggregate the features from all parts. Then the aggregated GNN features are used to compute frequency coefficients (orange) which later modulate the feature transformation of point x (green). Finally, density σ and appearance c is predicted as in NeRF.

3.1 Part-relative pose encoding

Inspired by DANBO (Su et al., 2022), we adopt a graph representation for the human skeleton, where each node corresponds to a joint that is linked to neighboring joints by bones. For a given pose with N_B joints $\theta = [\omega_1, \omega_2, \ldots, \omega_{N_B}]$, where $\omega_i \in \mathbb{R}^6$ (Zhou et al., 2019) is the rotation parameter of bone $i \in \{1, 2, \ldots, N_B\}$, we regress a feature vector for each bone part as:

$$[G_1, G_2, \ldots, G_{N_B}] = \mathrm{GNN}(\theta), \tag{1}$$

where GNN represents a learnable graph neural network. To process the irregular human skeleton, we employ two graph convolutional layers, followed by per-node 2-layer Multi-Layer Perceptrons (MLPs). To account for the irregular nature of human skeleton nodes, we learn individual MLP weights for each node; see (Su et al., 2022) for more comprehensive details.

Given a sample location $x \in \mathbb{R}^3$ in global coordinates for which the NeRF should output color and density, we first map it to the i-th bone-relative space as

$$\begin{bmatrix} \hat{x}_i \\ 1 \end{bmatrix} = T(\omega_i) \begin{bmatrix} x \\ 1 \end{bmatrix}, \tag{2}$$

where $T(\omega_i)$ denotes the world-to-bone coordinates transformation matrix computed by the rotation parameter ω_i. We first perform a validness test for the scaled relative positions $\{\bar{x}_i = s_i \cdot \hat{x}_i\}$, where s_i is a learnable scaling factor to control the size of the volume the i-th part contributes to. This facilitates the processing efficiency and concentrates the network on local patterns. If no $\{\bar{x}_i\}$ falls in $[-1, 1]$, x is estimated to locate far from the body surface and is discarded. Then these features are employed to drive the frequency modulation adaptively.

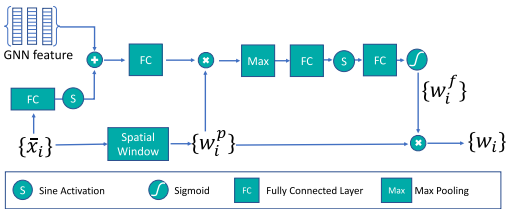

Figure 3: **Learned window function**. The query point location is processed with a spatial and pose-dependent window to remove spurious correlations between distant joints.

3.2 Frequency Modulation

Two-stage Window Function. To decide which per-part point-wise features to pass on to the downstream network and address the feature aggregation issues in (Su et al., 2022), we design a learnable two-stage window function. In Fig. 3, the window function takes the per-part GNN feature set $\{G_i\}$ and the scaled relative position set $\{\bar{x}_i\}$ of a valid point x as inputs. To facilitate learning volume dimensions $\{s_i\}$ that adapt to the body shape and to mitigate seam artifacts, we define

$$w_i^p = \exp(-\alpha(\|\bar{x}_i\|_2^\beta)), \tag{3}$$

where $\|\cdot\|_2$ is the L_2-norm. The w_i^p function attenuates the extracted feature based on the relative spatial distances to the bone centers such that multiple volumes are separated via the spatial similarities between x and the given parts. Thus we name w_i^p as the spatial window function. We set $\alpha = 2$ and $\beta = 6$ as in (Lombardi et al., 2021). However, it is possible that one part might prioritize

over other parts when multiple valid parts' feature space overlap. This motivates us to take the pose context into account and consider the point-wise feature of each part as the second stage. First, we perform $\dot{x}_i = \sin(\mathbf{W}_c \cdot \bar{x}_i)$ for each $\bar{x}_i$, where $\mathbf{W}_c$ indicates a Gaussian initialized fully-connected layer as in FFN (Tancik et al., 2020). After concatenating $\{\dot{x}_i\}$ and the GNN features $\{G_i\}$ correspondingly, we apply a full-connected layer to regress $\{f_i^p\}$ as the point-wise feature of the i-th part. Then we attenuate the feature as $f_i^w = f_i^p \cdot w_i^p$ to focus on spatially nearby parts.

To further decide which part x belongs to, we compute relative weights by aggregating all $\{f_i^w\}$ through a max pooling for the holistic shape-level representation. The max-pooled feature is fed into a sequence of fully-connected layers which are activated by a Sigmoid function to output a per-part weight w_i^f. We call the feature window function w_i^f to echo the spatial window function w_i^p since it operates on pose features. Finally, we compute the per-part weight $w_i = w_i^p \cdot w_i^f$ and output modulation frequencies as

$$f^m = \sum_{i=0}^{N_B} w_i \cdot G_i, \quad [\theta_1, \theta_2, \cdots, \theta_n] = \text{MLP}\ (f^m), \tag{4}$$

where f^m, θ_i and n represent the aggregated part feature, the modulation frequency coefficient at i-th layer and the layer number of the subsequent modulation module, respectively.

After the two-stage window function, the extracted f^m sparsely correspond to a small part set. To echo the locality assumption throughout the entire network, we also perform the window function w_i for the N_B relative positions of query point x as $\{\tilde{x}_i = \bar{x}_i \cdot w_i\}$. Note that, we aggregate the part features before MLP-based frequency modulation to avoid time-consuming processing over all parts for all samples. Thus computation complexity reduces significantly.

Frequency Prediction. Inspired by pi-GAN (Chan et al., 2021), we build the backbone network for each x with a series of Sine-activated fully-connected layers (Sitzmann et al., 2020). To this end, we first concatenate all the re-weighed positions $\{\tilde{x}_i\}$ as a whole and input it into a Sine-activated fully-connected layer (Sitzmann et al., 2020). Later on, each fully-connected layer is defined as

$$\mathbf{f}_i = \sin(\theta_i \cdot \mathbf{W}_i \mathbf{f}_{i-1} + \mathbf{b}_i), \tag{5}$$

where $\mathbf{W}_i$ and $\mathbf{b}_i$ are trainable weight and bias in the i-th layer L_i. Finally, we concatenate the Sine-activated features $\{\mathbf{f}_i\}$ as $S(x) = [\mathbf{f}_1, \mathbf{f}_2, \cdots, \mathbf{f}_n]$ for further processing.

Design Discussions and relation to DANBO. Both our method and DANBO (Su et al., 2022) use the GNN features as a building block to measure bone correlations. By contrast to DANBO which directly estimates part-level feature spaces from GNN features, we leverage these aggregated GNN features to estimate the appropriate frequencies, driving the frequency modulation for the input positions. This enables the linked MLP networks to adaptively capture a wide spectrum of coarse and fine details with high variability, as illustrated in the visual comparisons to DANBO in Fig. 1, 4, 5, 6. Moreover, although some work (Hertz et al., 2021; Wu et al., 2023) aims to modulate frequency features with locality, we make the first step for pose-dependent frequency modulation, which is critical in human avatar modeling. We start from existing conceptual components, analyze their limitations, and propose a novel solution. Specifically, we focus on how to connect GNN pose embeddings with frequency transformations. We then propose a simple window function to improve efficiency without losing accuracy which is also special and helpful in neural avatar modeling.

3.3 Volume Rendering and Loss Functions

The output feature $S(x)$ can accurately capture the information of pose dependency and spatial positions, and thus enables adaptive pattern synthesis. To obtain high-quality human body, we learn a neural field F to predict the color c and density σ at position x as

$$(\mathbf{c}, \sigma) = F(S(x), r), \tag{6}$$

where $r \in \mathbb{R}^2$ indicates the given ray directions. Following the existing neural radiance rendering pipelines for human avatars (Su et al., 2021; 2022; Wang et al., 2022), we output the image of the human subject as in the original NeRF:

$$\hat{C}\left(r\right) = \sum_{i=1}^{n} \mathcal{T}_i \left(1 - \exp(-\sigma_i \delta_i)\right) \mathbf{c}_i, \mathcal{T}_i = \exp(-\sum_{j=1}^{i-1} \sigma_j \delta_j). \tag{7}$$

Figure 4: **Visual comparisons on MonoPerfCap.** We can preserve better shape contours (1st row) and produce realistic cloth textures without artifacts (highlighted by the red arrow on 2nd row).

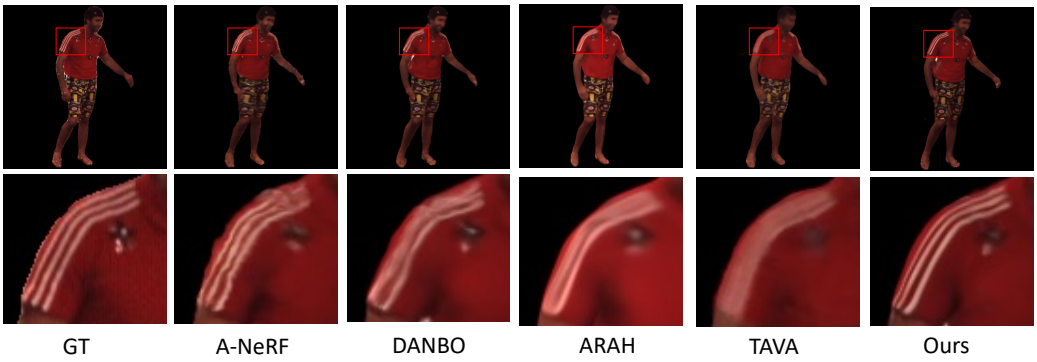

Figure 5: **Visual comparisons for novel view synthesis.** Compared to baselines, we can vividly reproduce the structured patterns.

Here, $\hat{C}$ and δ_i indicate the synthesized image and the distance between adjacent samples along a given ray respectively. Finally, we compute the L_1 loss $\|\cdot\|_1$ for training as

$$\mathcal{L}_{rec} = \sum_{\mathbf{r}\in\mathfrak{R}} \left\| \hat{C}(r) - C_{gt}(r) \right\|_1, \tag{8}$$

where $\mathfrak{R}$ is the whole ray set and C_{gt} is the ground truth. The usage of L_1 loss is to enable more robust network training. Following (Lombardi et al., 2021), we add a regularization loss on the scaling factors to prevent the per-bone volumes from growing too large and taking over other volumes:

$$\mathcal{L}_{\text{s}} = \sum_{i=1}^{N_B} (s_i^x \cdot s_i^y \cdot s_i^z), \tag{9}$$

where $\{s_i^x, s_i^y, s_i^z\}$ are the scaling factors along $\{x, y, z\}$ axes respectively. Hence, our total loss with weight λ_s is

$$\mathcal{L} = \mathcal{L}_{rec} + \lambda_s \mathcal{L}_{\text{s}}. \tag{10}$$

4 Results

In this section, we compare our approach with several state-of-the-art methods, including Neural-Body (Peng et al., 2021b), Anim-NeRF (Peng et al., 2021a), A-NeRF (Su et al., 2021), TAVA (Li et al., 2022a), DANBO (Su et al., 2022), and ARAH (Wang et al., 2022). These methods vary in their utilization of surface-free, template-based, or scan-based priors. We also conduct an ablation study to assess the improvement achieved by each network component. This study analyzes and discusses the effects of the learnable window function. Source code will be released with the publication.

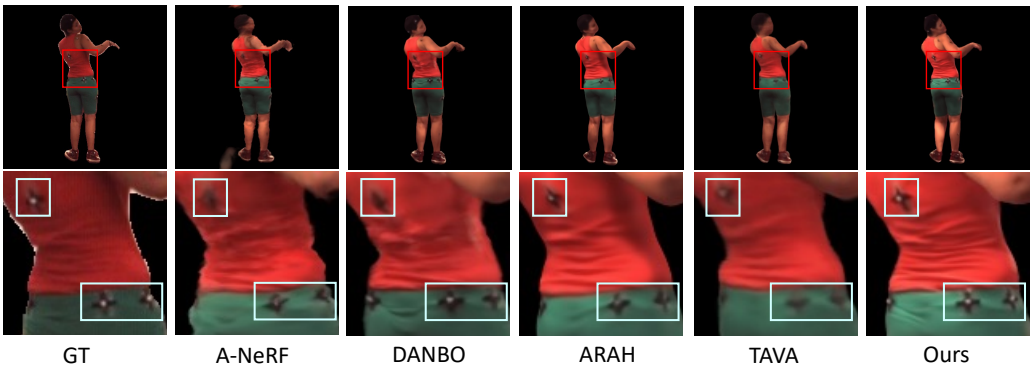

Figure 6: **Visual comparisons for novel pose rendering.** For novel poses that are unseen during training, cloth wrinkles form chaotically. Hence, none of the methods is expected to match the folds. Ours yields the highest detail, including the highlighted marker texture.

Table 1: **(a) Unseen pose synthesis on MonoPerfCap Xu et al. (2018)**. Our full model shows better overall perceptual quality over chosen models from monocular videos. **(b) Ablation studies on Human3.6M S9.** Our full model outperforms all ablated baselines across all metrics.

	ND		WP		Avg	
	PSNR↑	SSIM↑	PSNR↑	SSIM↑	PSNR↑	SSIM↑
onlyGNN	20.03	0.841	22.71	0.863	21.37	0.852
onlySyn	19.57	0.827	22.66	0.860	21.12	0.844
DANBO	20.10	0.842	22.39	0.861	21.25	0.852
Ours	**20.55**	**0.853**	**22.85**	**0.866**	**21.70**	**0.860**

(a)

	onlyGNN	noGNN	onlySyn	*only* w_i^p	*only* w_i^f	*no window*	Ours (full)
Novel view							
PSNR↑	25.91	26.08	25.86	26.21	25.91	22.21	**26.39**
SSIM↑	0.917	0.925	0.916	0.925	0.921	0.639	**0.929**
LPIPS↓	0.120	0.105	0.118	0.112	0.124	0.478	**0.100**
Novel pose							
PSNR↑	24.75	24.45	24.82	25.01	24.72	20.98	**25.12**
SSIM↑	0.891	0.899	0.901	0.904	0.900	0.628	**0.908**
LPIPS↓	0.146	0.131	0.141	0.133	0.148	0.502	**0.122**

(b)

4.1 Experimental Settings

We evaluate our method on widely recognized benchmarks for body modeling. Following the protocol established by Anim-NeRF, we perform comparisons on the seven actors of the Human3.6M dataset (Ionescu et al., 2011; 2013; Peng et al., 2021a) using the method described in (Gong et al., 2018) to compute the foreground maps. Like DANBO, we also apply MonoPerfCap (Xu et al., 2018) as a high-resolution dataset to evaluate the robustness to unseen poses in monocular videos.

To ensure a fair comparison, we follow the previous experimental settings including the dataset split and used metrics (Su et al., 2021; 2022; Li et al., 2022a). Specifically, we utilize standard image metrics such as pixel-wise Peak Signal-to-Noise Ratio (PSNR) and Structural Similarity Index Metric (SSIM) (Wang et al., 2004) to evaluate the quality of output images. Additionally, we employ perceptual metrics like the Learned Perceptual Image Patch Similarity (LPIPS) (Zhang et al., 2018) to assess the structural accuracy and textured details of the generated images. Since our primary focus is on the foreground subjects rather than the background image, we report the scores based on tight bounding boxes, ensuring the evaluation to be focused on the relevant regions of interest.

4.2 Novel View Synthesis

To evaluate the generalization capability under different camera views, we utilize multi-view datasets where the body model is learned from a subset of cameras. The remaining cameras are then utilized as the test set, allowing us to render the same pose from unseen view directions.

We present the visual results in Fig. 5. Comparing to the selected baselines, our method shows superior performance in recovering fine-grained details, as evident in the examples such as the stripe texture depicted on the first row. We attribute this to the explicit frequency modulation which mitigates grainy artifacts and overly smooth regions. Tab. 2 quantifies our method's empirical advantages, supporting our previous findings.

Figure 7: **Ablation studies** on sub-branch networks (a) and on window functions (b). Only the full model can faithfully synthesize the structured patterns (e.g. the strip textures) in (a) and avoid artifacts and contour distortions in (b).

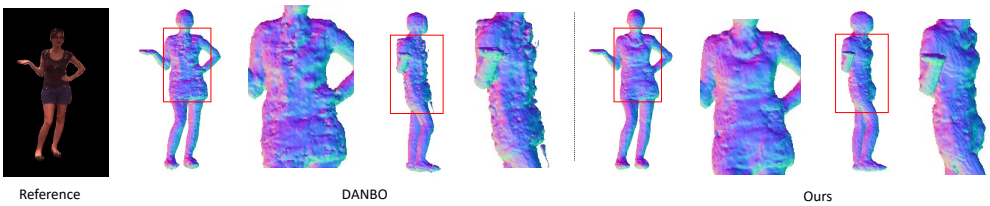

Figure 8: **Geometry reconstruction.** Our method yields more precise, less noisy shape estimates. Some noise remains as no template mesh or other surface prior is used.

4.3 Novel Pose Rendering

We follow prior work and measure the quality of novel pose synthesis by training on the first part of a video and testing on the remaining frames. Only the corresponding 3D pose is used as input. This tests the generalization of the learned pose modulation strategy and applicability to animation.

We present the visual comparisons for the Human3.6M dataset in Fig. 6, where our method demonstrates superior results than baselines in terms of fine-grained and consistent renderings. Specifically, our method generates sharper details such as those seen in wrinkles and better texture consistency, as exemplified by the clearer marker (highlighted by boxes). Tab. 2 further quantitatively verifies that our method generalizes well to both held-out poses and out-of-distribution poses across the entire test set. Please note that none of the methods matches wrinkle locations perfectly, as these form chaotically, dependent on the past motion, not just on the single frame used by all methods for conditioning. Learning such motion dynamics remains an open problem that is orthogonal to learning pose-dependent detail.

Moreover, we provide the visual comparisons in Fig. 4 and the quantitative metrics in Tab. 1 (a) for the high-resolution outdoor monocular video sequences MonoPerfCap (Xu et al., 2018). Being consistent with the results on the Human3.6M sequences, our method presents better capability in learning a generalized model from monocular videos.

Furthermore, we test the animation ability of our approach by driving models learned from the Human3.6M dataset with extreme out-of-distribution poses from AIST (Li et al., 2021a). The qualitative results shown in Fig. 9 validate that even under extreme pose variation our approach produces plausible body shapes with desired texture details while the baseline show severe artifacts. Here no quantitative evaluations are performed since no ground truth data is available.

Table 2: **Novel-view and novel-pose synthesis results, averaged over the Human3.6M test set.** Our method benefits from the explicit frequency modulations, yielding better perceptual quality, reaching the best overall score in all metrics.

	Novel view			Novel pose		
	PSNR↑	SSIM↑	LPIPS↓	PSNR↑	SSIM↑	LPIPS↓
Template/Scan-based prior						
NeuralBody	23.36	0.905	0.140	22.81	0.888	0.157
Anim-NeRF	23.34	0.897	0.157	22.61	0.881	0.170
ARAH†	24.63	0.920	0.115	23.27	0.897	0.134
Template-free						
A-NeRF	24.26	0.911	0.129	23.02	0.883	0.171
DANBO	24.69	0.917	0.116	23.74	0.901	0.131
TAVA	24.72	0.919	0.124	23.52	0.899	0.141
Ours	**25.06**	**0.921**	**0.110**	**24.15**	**0.906**	**0.124**

†: using public release that differs to Wang et al. (2022).

4.4 Geometry Visualization

In Fig. 8, we analyze the geometry reconstructed with our approach against reconstructions from the baseline. Our method captures better body shapes and per-part geometry. Specifically, our results

Figure 9: **Animation capability.** Our method maintains the reconstructed high frequency details when retargeting and creates fewer artifacts, lending itself for retargeting.

present overall more complete body outline and a smoother surface. In contrast, the baselines predict more noisy blobs near the body surface. Together with the results of novel view and novel pose synthesis, we also attribute our more consistent rendering results across novel views than the baselines to better geometry preservation. This might suggest that more faithful modeling of geometry is also beneficial for the visual fidelity as shown in the appended video.

4.5 Ablation Study Results

To test the significance of each component, we conduct the ablation study on all Human3.6M sequences with six ablated models: **1.** Only preserve the upper branch network with GNN features as onlyGNN; **2.** Only preserve the bottom branch network without frequency modulation as onlySyn; **3.** For the two-stage window function, we only preserve w_i^p to evaluate the effectiveness of the spatial similarities between x and all bone parts as $\text{only } w_i^p$; **4.** We only preserve w_i^f for the importance of max-pooled object-level feature as $\text{only } w_i^f$; **5.** We remove the whole window function as no window. **6.** We concatenate all pose parameters into one vector and replace the GNN layers with one single MLP to evaluate the effectiveness of per-part modeling as noGNN; see Fig. 15 for detailed architecture. In Fig. 7,we present the qualitative ablation study results for S9. Specifically, the onlyGNN model is prone to produce blurry textures due to its low frequency bias while the onlySyn model introduces noisy artifacts near stripe textures. Similar to onlySyn, the noGNN model blurs the stripe patterns with noisy artifacts. Only the combination yields their full advantage and successfully synthesizes structured patterns, as shown in Fig. 7 (a). As mentioned in method section, w_i^p and w_i^f cater for the relationships in position space and feature space, respectively. As shown by the results of novel pose rendering (Fig. 7 (b)), neither using w_i^p or w_i^f alone suffices to produce the image quality of the full model, demonstrating the necessity of all contributions. Tab. 1 (b) lists our corresponding quantitative results of all sequences to further support our statement.

Tab. 1 (a) presents the quantitative scores from the MonoPerfCap dataset, showcasing the performance of both the onlyGNN and onlySyn models. Similar to the result differences shown in Tab. 1 (b), our full model consistently outperforms these two ablated models, which reveals our full model's adaptability to diverse in-the-wild scenarios depicted in high-resolution images. With all these results, we conclude that each component clearly contribute to the empirical success of the full model. More ablation studies on the pose-dependent frequency modulation can be found in the appendix.

5 Conclusion

We introduce a novel, frequency-based framework based on NeRF (Mildenhall et al., 2020) that enables the accurate learning of human body representations from videos. The main contribution of our approach is the explicit integration of desired frequency modeling with pose context. When compared to state-of-the-art algorithms, our method demonstrates improved synthesis quality and enhanced generalization capabilities, particularly when faced with unseen poses and camera views.

Acknowledgements This work was supported by the Natural Sciences and Engineering Research Council of Canada (NSERC) Discovery Grant and by Advanced Research Computing at the University of British Columbia. We thank Shih-Yang Su for his help and discussions. We also thank ARC at UBC and Compute Canada for providing computational resources.

REFERENCES

Abien Fred Agarap. Deep learning using rectified linear units (relu). *CoRR*, 2018.

Timur Bagautdinov, Chenglei Wu, Tomas Simon, Fabian Prada, Takaaki Shiratori, Shih-En Wei, Weipeng Xu, Yaser Sheikh, and Jason Saragih. Driving-signal aware full-body avatars. *ACM TOG*, 2021.

Ang Cao and Justin Johnson. Hexplane: A fast representation for dynamic scenes. In *CVPR*, 2023.

Eric R Chan, Marco Monteiro, Petr Kellnhofer, Jiajun Wu, and Gordon Wetzstein. pi-gan: Periodic implicit generative adversarial networks for 3d-aware image synthesis. In *CVPR*, 2021.

Liang-Chieh Chen, George Papandreou, Florian Schroff, and Hartwig Adam. Rethinking atrous convolution for semantic image segmentation. 2017.

Xu Chen, Yufeng Zheng, Michael J Black, Otmar Hilliges, and Andreas Geiger. Snarf: Differentiable forward skinning for animating non-rigid neural implicit shapes. In *ICCV*, 2021.

Boyang Deng, John P Lewis, Timothy Jeruzalski, Gerard Pons-Moll, Geoffrey Hinton, Mohammad Norouzi, and Andrea Tagliasacchi. Nasa neural articulated shape approximation. In *ECCV*, 2020.

Junting Dong, Qi Fang, Yudong Guo, Sida Peng, Qing Shuai, Xiaowei Zhou, and Hujun Bao. Totalselfscan: Learning full-body avatars from self-portrait videos of faces, hands, and bodies. In *NeurIPS*, 2022.

Yilun Du, Yinan Zhang, Hong-Xing Yu, Joshua B Tenenbaum, and Jiajun Wu. Neural radiance flow for 4d view synthesis and video processing. In *ICCV*, 2021.

Rizal Fathony, Anit Kumar Sahu, Devin Willmott, and J Zico Kolter. Multiplicative filter networks. In *ICLR*, 2021.

Chen Gao, Ayush Saraf, Johannes Kopf, and Jia-Bin Huang. Dynamic view synthesis from dynamic monocular video. In *ICCV*, 2021.

Ke Gong, Xiaodan Liang, Yicheng Li, Yimin Chen, Ming Yang, and Liang Lin. Instance-level human parsing via part grouping network. In *ECCV*, 2018.

Chen Guo, Tianjian Jiang, Xu Chen, Jie Song, and Otmar Hilliges. Vid2avatar: 3d avatar reconstruction from videos in the wild via self-supervised scene decomposition. In *CVPR*, 2023.

Amir Hertz, Or Perel, Raja Giryes, Olga Sorkine-Hornung, and Daniel Cohen-Or. Sape: Spatially-adaptive progressive encoding for neural optimization. *NeurIPS*, 2021.

Hao Hu, Dongsheng Xiao, Helge Rhodin, and Timothy H Murphy. Towards a visualizable, de-identified synthetic biomarker of human movement disorders. *Journal of Parkinson's Disease*, 2022.

Catalin Ionescu, Fuxin Li, and Cristian Sminchisescu. Latent structured models for human pose estimation. In *ICCV*, 2011.

Catalin Ionescu, Dragos Papava, Vlad Olaru, and Cristian Sminchisescu. Human3. 6m: Large scale datasets and predictive methods for 3d human sensing in natural environments. *IEEE TPAMI*, 2013.

Wei Jiang, Kwang Moo Yi, Golnoosh Samei, Oncel Tuzel, and Anurag Ranjan. Neuman: Neural human radiance field from a single video. In *ECCV*, 2022.

Diederik P Kingma and Jimmy Ba. Adam: A method for stochastic optimization. *ICLR*, 2014.

Nikos Kolotouros, Georgios Pavlakos, Michael J Black, and Kostas Daniilidis. Learning to reconstruct 3d human pose and shape via model-fitting in the loop. In *ICCV*, 2019.

Youngjoong Kwon, Dahun Kim, Duygu Ceylan, and Henry Fuchs. Neural human performer: Learning generalizable radiance fields for human performance rendering. *NeurIPS*, 2021.

Ruilong Li, Shan Yang, David A Ross, and Angjoo Kanazawa. Ai choreographer: Music conditioned 3d dance generation with aist++. In *ICCV*, 2021a.

Ruilong Li, Julian Tanke, Minh Vo, Michael Zollhöfer, Jürgen Gall, Angjoo Kanazawa, and Christoph Lassner. Tava: Template-free animatable volumetric actors. In *ECCV*, 2022a.

Tianye Li, Mira Slavcheva, Michael Zollhoefer, Simon Green, Christoph Lassner, Changil Kim, Tanner Schmidt, Steven Lovegrove, Michael Goesele, Richard Newcombe, et al. Neural 3d video synthesis from multi-view video. In *CVPR*, 2022b.

Zhe Li, Zerong Zheng, Yuxiao Liu, Boyao Zhou, and Yebin Liu. Posevocab: Learning joint-structured pose embeddings for human avatar modeling. In *SIGGRAPH*, 2023.

Zhengqi Li, Simon Niklaus, Noah Snavely, and Oliver Wang. Neural scene flow fields for space-time view synthesis of dynamic scenes. In *CVPR*, 2021b.

David B Lindell, Dave Van Veen, Jeong Joon Park, and Gordon Wetzstein. BACON: Band-limited Coordinate Networks for Multiscale Scene Representation. *CVPR*, 2022.

Lingjie Liu, Marc Habermann, Viktor Rudnev, Kripasindhu Sarkar, Jiatao Gu, and Christian Theobalt. Neural actor: Neural free-view synthesis of human actors with pose control. *ACM TOG*, 2021.

Stephen Lombardi, Tomas Simon, Gabriel Schwartz, Michael Zollhoefer, Yaser Sheikh, and Jason Saragih. Mixture of volumetric primitives for efficient neural rendering. *ACM TOG*, 2021.

Matthew Loper, Naureen Mahmood, Javier Romero, Gerard Pons-Moll, and Michael J Black. Smpl: A skinned multi-person linear model. *ACM TOG*, 2015.

Ishit Mehta, Michaël Gharbi, Connelly Barnes, Eli Shechtman, Ravi Ramamoorthi, and Manmohan Chandraker. Modulated Periodic Activations for Generalizable Local Functional Representations. In *ICCV*, 2021.

Ben Mildenhall, Pratul P Srinivasan, Matthew Tancik, Jonathan T Barron, Ravi Ramamoorthi, and Ren Ng. Nerf: Representing scenes as neural radiance fields for view synthesis. *ECCV*, 2020.

Atsuhiro Noguchi, Xiao Sun, Stephen Lin, and Tatsuya Harada. Neural articulated radiance field. 2021.

Keunhong Park, Utkarsh Sinha, Jonathan T Barron, Sofien Bouaziz, Dan B Goldman, Steven M Seitz, and Ricardo Martin-Brualla. Nerfies: Deformable neural radiance fields. In *ICCV*, 2021a.

Keunhong Park, Utkarsh Sinha, Peter Hedman, Jonathan T. Barron, Sofien Bouaziz, Dan B Goldman, Ricardo Martin-Brualla, and Steven M. Seitz. Hypernerf: A higher-dimensional representation for topologically varying neural radiance fields. *ACM TOG*, 2021b.

Adam Paszke, Sam Gross, Francisco Massa, Adam Lerer, James Bradbury, Gregory Chanan, Trevor Killeen, Zeming Lin, Natalia Gimelshein, Luca Antiga, et al. Pytorch: An imperative style, high-performance deep learning library. 2019.

Sida Peng, Junting Dong, Qianqian Wang, Shangzhan Zhang, Qing Shuai, Xiaowei Zhou, and Hujun Bao. Animatable neural radiance fields for modeling dynamic human bodies. In *ICCV*, 2021a.

Sida Peng, Yuanqing Zhang, Yinghao Xu, Qianqian Wang, Qing Shuai, Hujun Bao, and Xiaowei Zhou. Neural body: Implicit neural representations with structured latent codes for novel view synthesis of dynamic humans. In *CVPR*, 2021b.

Albert Pumarola, Enric Corona, Gerard Pons-Moll, and Francesc Moreno-Noguer. D-nerf: Neural radiance fields for dynamic scenes. In *CVPR*, 2021.

Shunsuke Saito, Jinlong Yang, Qianli Ma, and Michael J Black. Scanimate: Weakly supervised learning of skinned clothed avatar networks. In *CVPR*, 2021.

Vincent Sitzmann, Julien Martel, Alexander Bergman, David Lindell, and Gordon Wetzstein. Implicit neural representations with periodic activation functions. *NeurIPS*, 2020.

Shih-Yang Su, Frank Yu, Michael Zollhöfer, and Helge Rhodin. A-nerf: Articulated neural radiance fields for learning human shape, appearance, and pose. *NeurIPS*, 2021.

Shih-Yang Su, Timur Bagautdinov, and Helge Rhodin. Danbo: Disentangled articulated neural body representations via graph neural networks. In *ECCV*, 2022.

Matthew Tancik, Pratul Srinivasan, Ben Mildenhall, Sara Fridovich-Keil, Nithin Raghavan, Utkarsh Singhal, Ravi Ramamoorthi, Jonathan Barron, and Ren Ng. Fourier Features Let Networks Learn High Frequency Functions in Low Dimensional Domains. *NeurIPS*, 2020.

Justus Thies, Michael Zollhöfer, and Matthias Nießner. Deferred neural rendering: Image synthesis using neural textures. *ACM TOG*, 2019.

Edgar Tretschk, Ayush Tewari, Vladislav Golyanik, Michael Zollhöfer, Christoph Lassner, and Christian Theobalt. Non-rigid neural radiance fields: Reconstruction and novel view synthesis of a dynamic scene from monocular video. In *ICCV*, 2021.

Peng Wang, Lingjie Liu, Yuan Liu, Christian Theobalt, Taku Komura, and Wenping Wang. Neus: Learning neural implicit surfaces by volume rendering for multi-view reconstruction. In *NeurIPS*, 2021.

Shaofei Wang, Katja Schwarz, Andreas Geiger, and Siyu Tang. Arah: Animatable volume rendering of articulated human sdfs. In *ECCV*, 2022.

Zhou Wang, Alan C Bovik, Hamid R Sheikh, and Eero P Simoncelli. Image quality assessment: from error visibility to structural similarity. *IEEE TIP*, 2004.

Chung-Yi Weng, Brian Curless, Pratul P Srinivasan, Jonathan T Barron, and Ira Kemelmacher-Shlizerman. HumanNeRF: Free-viewpoint Rendering of Moving People from Monocular Video. In *CVPR*, 2022.

Zhijie Wu, Xiang Wang, Di Lin, Dani Lischinski, Daniel Cohen-Or, and Hui Huang. Sagnet: Structure-aware generative network for 3d-shape modeling. *ACM TOG*, 2019.

Zhijie Wu, Yuhe Jin, and Kwang Moo Yi. Neural fourier filter bank. In *CVPR*, 2023.

Yiheng Xie, Towaki Takikawa, Shunsuke Saito, Or Litany, Shiqin Yan, Numair Khan, Federico Tombari, James Tompkin, Vincent Sitzmann, and Srinath Sridhar. Neural Fields in Visual Computing and Beyond. *Computer Graphics Forum*, 2022.

Weipeng Xu, Avishek Chatterjee, Michael Zollhöfer, Helge Rhodin, Dushyant Mehta, Hans-Peter Seidel, and Christian Theobalt. Monoperfcap: Human performance capture from monocular video. *ACM TOG*, 2018.

Zhengming Yu, Wei Cheng, Xian Liu, Wayne Wu, and Kwan-Yee Lin. Monohuman: Animatable human neural field from monocular video. In *CVPR*, 2023.

Wentao Yuan, Zhaoyang Lv, Tanner Schmidt, and Steven Lovegrove. Star: Self-supervised tracking and reconstruction of rigid objects in motion with neural rendering. In *CVPR*, 2021.

Richard Zhang, Phillip Isola, Alexei A Efros, Eli Shechtman, and Oliver Wang. The unreasonable effectiveness of deep features as a perceptual metric. In *CVPR*, 2018.

Zerong Zheng, Han Huang, Tao Yu, Hongwen Zhang, Yandong Guo, and Yebin Liu. Structured local radiance fields for human avatar modeling. In *CVPR*, 2022.

Zerong Zheng, Xiaochen Zhao, Hongwen Zhang, Boning Liu, and Yebin Liu. Avatarrex: Real-time expressive full-body avatars. *ACM TOG*, 2023.

Yi Zhou, Connelly Barnes, Jingwan Lu, Jimei Yang, and Hao Li. On the continuity of rotation representations in neural networks. In *CVPR*, 2019.

Appendices

In this part, we first present the details about method implementation, used dataset and data split. Then we provide more comparison results on the frequency histograms, geometry visualization and motion retargeting. We also attach more ablation studies to emphasize the significance of pose-guided frequency modulation and window functions. More qualitative results for novel view synthesis and novel pose rendering are provided as well. Finally, we discuss the limitations and social impacts of this project. See the attached video for the animation and geometry visualization results.

A Implementation Details

For consistency, we maintain the same hyper-parameter settings across various testing experiments, including the loss function with weight λ_{s}, the number of training iterations, and the network capacity and learning rate. All the hyper-parameters are chosen depending on the final accuracy on chosen benchmarks. Our method is implemented using PyTorch (Paszke et al., 2019). We utilize the Adam optimizer (Kingma & Ba, 2014) with default parameters $\beta_1 = 0.9$ and $\beta_2 = 0.99$. We employ the step decay schedule to adjust the learning rate, where the initial learning rate is set to 5×10^{-4} and we drop the learning rate to 10% every 500000 iterations. Like former methods (Su et al., 2021; 2022), we set $\lambda_{\text{s}} = 0.001$ and $N_B = 24$ to accurately capture the topology variations and avoid introducing unnecessary training changes. The learnable parameters in GNN, window function and the frequency modulation part are activated by the Sine function while other parameters in the neural field F are activated by Relu (Agarap, 2018). We train our network on a single NVidia RTX 3090 GPU for about 20 hours.

B More Details about Datasets

Follow the experimental settings of previous methods (Su et al., 2021; 2022), we choose the Human3.6M (Ionescu et al., 2011) and MonoPerfCap (Xu et al., 2018) as the evaluation benchmarks. These datasets cover the indoor and outdoor scenes captured by monocular and multi-view videos. Specifically, we use a total of 7 subjects for evaluation under the same evaluation protocol as in AnimNeRF (Peng et al., 2021a). We compute the foreground images with (Gong et al., 2018) to focus on the target characters. Likewise, we adopt the identical pair of sequences and configuration as employed in A-NeRF (Su et al., 2021): Weipeng and Nadia, consisting of 1151 and 1635 images each, with a resolution of 1080×1920. We estimate the human and camera poses using SPIN (Kolotouros et al., 2019) and following pose refinement (Su et al., 2021). We apply the released DeepLabv3 model (Chen et al., 2017) to estimate the foreground masks. The data split also stays the same as the aforementioned methods for a fair comparison.

C More Results

Histogram Comparisons. Showing the frequency histograms of different frames, like the Fig. 1 in the main text, appear to be a clear solution to demonstrate our motivation. Thus we provide more examples and corresponding analysis here. Using the two close-ups in Fig. 1 of the main text, we present the corresponding frequency histograms for each method in Fig. 10. To test our effectiveness when training over long sequences, we provide the histogram results of two frames collected in the ZJU-MoCap (Peng et al., 2021b) dataset, in Fig. 11. Compared to DANBO, our method can produce more similar contours to the ground truth histograms. Additionally, the matched histogram distances (shown below the histogram subfigures and denoted as **F-Dist**) further confirm our advantages of producing adaptive frequency distributions which is the key point of our method.

Besides measuring the holistic histogram similarities, we directly compute a frequency map by regarding the standard deviation (STD) value at each pixel as a gray-scale value. As evidenced in Fig. 11, our method provides significantly improved results, as represented by the error images between the output frequencies and the ground truth values. All these results reveal that our method can faithfully reconstruct the desired frequency distributions both locally and holistically.

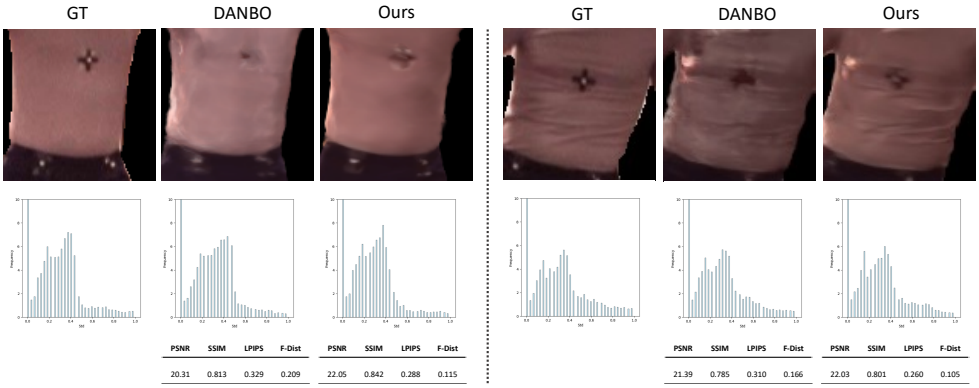

Figure 10: **Motivation Demonstration on Human3.6M frames.** Using the two frames in Fig. 1 of the main text, we present the frequency histograms, compute three image quality metrics (e.g. PSNR, SSIM, LPIPS) and the distances between the output frequency map and ground truth values (F-Dist) to justify our pose-guided frequency modulation. Compared to DANBO which modulates frequencies implicitly, our method can synthesize higher-quality images with more adaptive frequency distributions across different pose contexts.

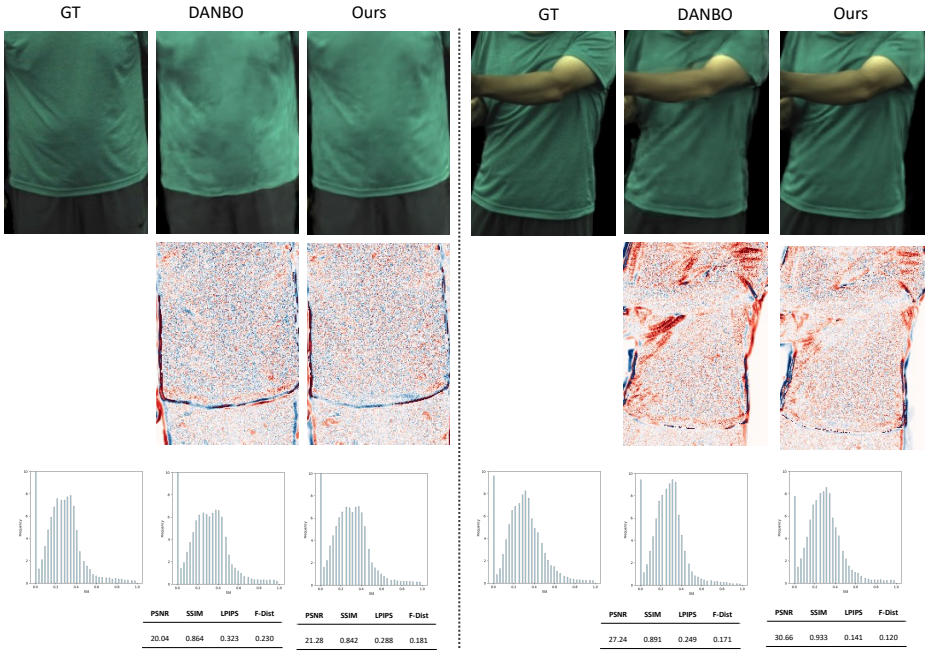

Figure 11: **Motivation Demonstration on ZJU-Mocap frames.** To test our effectiveness over long video sequences, we qualitatively and quantitatively evaluate our method with two ZJU-Mocap frames. Being consistent with the findings in Fig. 10, our method outperforms DANBO with more similar frequency histograms (3rd row) and better quantitative metrics on image quality and frequency modeling (last row). Additionally, we further illustrate the color-coded frequency error maps (2nd row) for both methods to show that our method can faithfully reconstruct the desired frequency distributions both locally and holistically. For the left frame with smooth patterns, our method introduces slightly few frequency errors as it is easy to model low-frequency variations. On the other hand, for the right frame with much more high-frequency wrinkles, our method faithfully reproduces the desired frequencies with significantly less errors, which clearly demonstrate the importance of our pose-guided frequency modulation. Here red denotes positive and blue denotes negative errors.

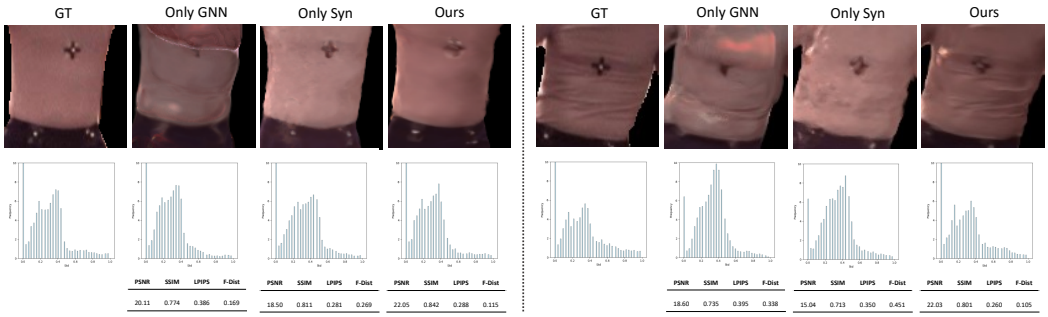

Figure 12: **Abaltion study on the network components with frequency analysis.** Our full model produces more adaptive frequency distributions and higher image quality than the ablated models.

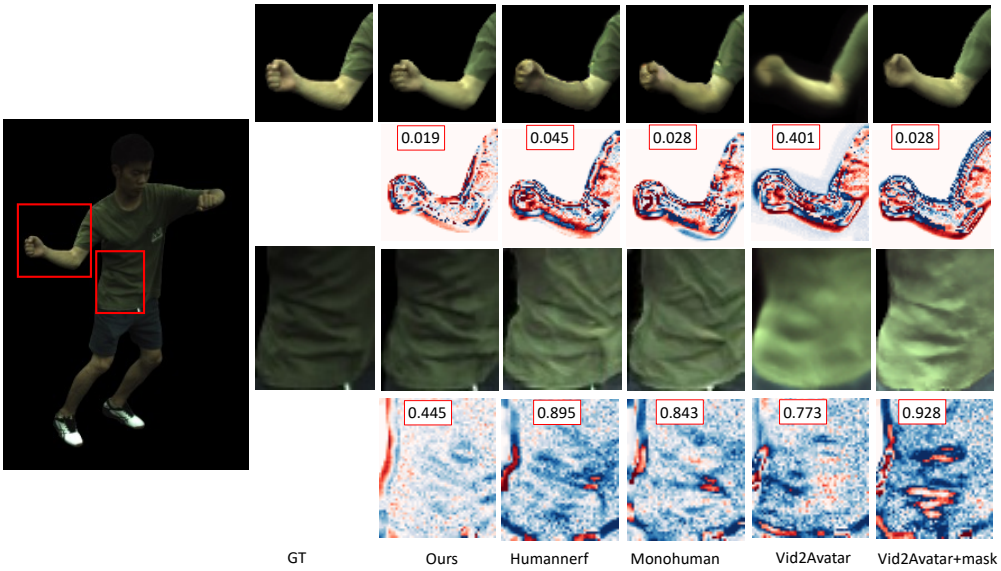

Figure 13: **Visual comparisons on ZJU-Mocap with modern baselines.** Among all methods, only our model can successfully synthesize the avatar fist with accurate arm contours (top row) and faithfully reconstruct the desired wrinkles (bottom row). In contrast, all baselines either distort or blur the fist patterns (top row) and clothing textures (bottom row). Additionally, the state-of-the-art methods fail to capture the cloth colors. Similar to Fig. 11, we illustrate the frequency error maps and compute the distances between the output frequency map and ground truth values (F-Dist). Being consistent with the findings in Fig. 10 and Fig. 11, the pose-guided frequency modulation can better reconstruct the desired frequency distributions both locally and holistically. Thus more adaptive patterns can be reproduced with reduced errors.

Table 3: **Novel-view synthesis results on the ZJU-Mocap Peng et al. (2021b) test set.** The pose-dependent frequency modulation facilitates generalizing to novel views with one single camera input. Here 'Vid2Avatar' indicates the original Vid2Avatar implementation while 'Vid2Avatar+mask' is the model only focusing on the foreground human representations, thus obtaining better metrics than the original version.

	S377		S387		S393		S394		Avg	
	PSNR	SSIM	PSNR	SSIM	PSNR	SSIM	PSNR	SSIM	PSNR	SSIM
NeuralBody	28.90	0.967	27.15	0.953	28.30	0.957	28.41	0.956	28.19	0.958
HumanNeRF	30.21	0.975	27.95	0.963	28.38	0.961	30.00	0.963	29.14	0.965
MonoHuman	30.23	0.976	**28.20**	0.962	28.40	0.962	30.02	0.963	29.21	0.966
Vid2Avatar	29.52	0.951	28.10	0.938	27.19	0.929	28.95	0.932	28.44	0.938
Vid2Avatar+mask	29.53	0.976	28.15	**0.965**	27.95	0.962	29.83	**0.965**	28.87	0.967
Ours	**30.72**	**0.979**	**28.20**	**0.965**	**28.91**	**0.964**	**30.36**	**0.965**	**29.55**	**0.968**

Table 4: **Novel pose rendering results on the ZJU-Mocap Peng et al. (2021b) test set.** Similar to Tab. 3, our method improves the quantitative results for novel pose rendering.

	S377		S387		S393		S394		Avg	
	PSNR	SSIM	PSNR	SSIM	PSNR	SSIM	PSNR	SSIM	PSNR	SSIM
NeuralBody	29.18	0.969	26.43	0.951	28.15	0.956	28.14	0.956	27.98	0.958
HumanNeRF	30.18	0.975	27.60	0.962	28.39	0.961	28.78	0.960	28.74	0.965
MonoHuman	30.26	0.977	27.66	0.961	28.78	0.962	29.11	0.961	28.95	0.965
Vid2Avatar	29.86	0.954	27.42	0.938	27.20	0.929	28.55	0.932	28.26	0.938
Vid2Avatar+mask	29.85	0.977	27.38	**0.964**	28.09	0.962	29.25	**0.963**	28.64	0.967
Ours	**30.95**	**0.979**	**27.71**	**0.964**	**28.96**	**0.964**	**29.60**	**0.963**	**29.31**	**0.968**

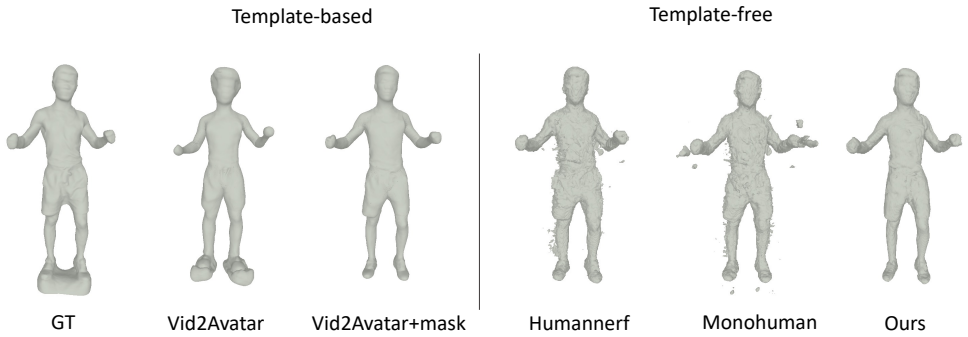

Figure 14: **Geometry reconstruction on ZJU-Mocap S377.** Compared to other template-free methods (HumanNeRF and MonoHuman), our method yields more precise and less noisy body shape. Some bumpy patterns remains as no template mesh or other surface prior is used, in contrast to Vid2Avatar.

Modern baselines on ZJU-Mocap sequences. To show our advantages with better generality, we train our method and three baselines, including HumanNeRF Weng et al. (2022), MonoHuman Yu et al. (2023), and Vid2Avatar Guo et al. (2023), over four ZJU-Mocap sequences (S377, S387, S393 and S394) following the experimental settings of HumanNeRF and MonoHuman. All results are achieved through their public codes with default hyper-parameters. Note that, we denote 'Vid2Avatar' as the original Vid2Avatar implementation and correspondingly 'Vid2Avatar+mask' as the model only focusing on the foreground human representations with better empirical results.

Table 5: **Geoemtry Reconstruction on the ZJU-Mocap Peng et al. (2021b) test set.** The pose-dependent frequency modulation improves template-free baselines with more faithful reconstruction and achieves similar results to template-based method.

	S377	S387	S393	S394	Avg
Template/Scan-based prior					
Vid2Avatar	0.1180	0.4696	0.3330	0.2480	0.2921
Vid2Avatar+mask	0.0336	0.0283	0.0404	0.0410	0.0359
Template-free					
HumanNeRF	0.0401	0.0777	0.0609	0.0543	0.0582
MonoHuman	0.0897	0.0801	0.0836	0.1006	0.0885
Ours	0.0337	0.0365	0.0455	0.0441	0.0400

Table 6: Ablation studies on full Human3.6M sequences. Our full model improves over all ablated baselines, showing the necessity of all components.

	onlyGNN	noGNN	onlySyn	*only* w_i^p	*only* w_i^f	*no window*	Ours (full)
Novel view							
PSNR↑	24.72	24.90	24.29	24.99	23.63	23.32	**25.06**
SSIM↑	0.914	0.918	0.911	0.920	0.835	0.842	**0.921**
LPIPS↓	0.125	0.112	0.124	0.110	0.272	0.305	**0.110**
Novel pose							
PSNR↑	23.72	23.64	23.74	24.00	22.97	22.42	**24.15**
SSIM↑	0.898	0.900	0.900	0.905	0.824	0.832	**0.906**
LPIPS↓	0.140	0.129	0.138	0.125	0.283	0.310	**0.124**

(b)

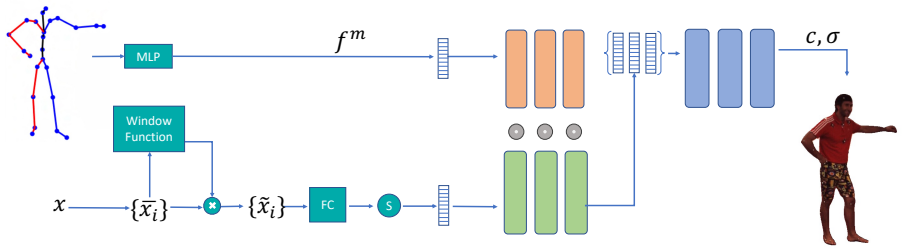

Figure 15: **Architecture of the ablated** noGNN **model.** Compared to our full model, we achieve noGNN by removing graph neural networks and directly feeding the joint parameters as a whole to one single Multi-Layer Perceptron (MLP) for frequency modulation.

In Fig. 13, we illustrate the visual comparisons for our method and chosen baselines. Both HumanNeRF and MonoHuman blur the highlighted avatar fist while we can faithfully reproduce the realistic patterns on the top row. Additionally, on the bottom, the pose-based frequency modulation enables smoother body contours and synthesizes more adaptive wrinkles (e.g. the wrinkle directions) while the baselines all fail to produce accurate cloth colors. The provided error images also underline that our method can more successfully simulate the ground truth images. Similar to Fig. 11, we compute the matched histogram distances (**F-Dist**) for the close-ups. The lowest frequency distance demonstrates that our method can best generate adaptive textures with appropriate frequency distributions. Thus better dynamic wrinkles are enabled. Tab. 3- 4 lists the metric comparisons for novel view synthesis and novel pose rendering, further championing our former observations.

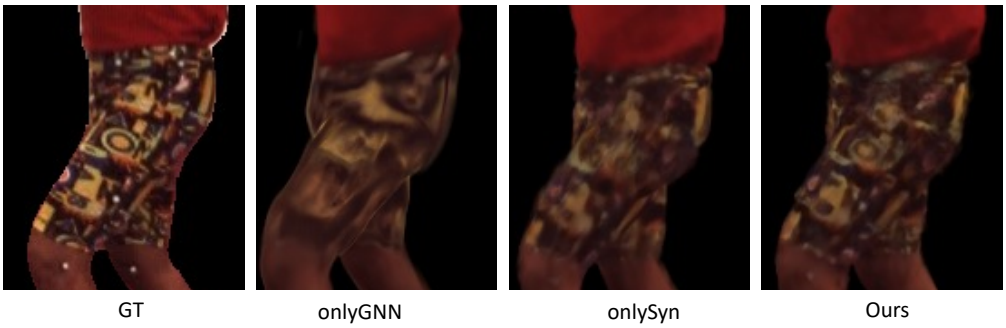

Figure 16: Ablation study on sub-branch networks with novel pose rendering.

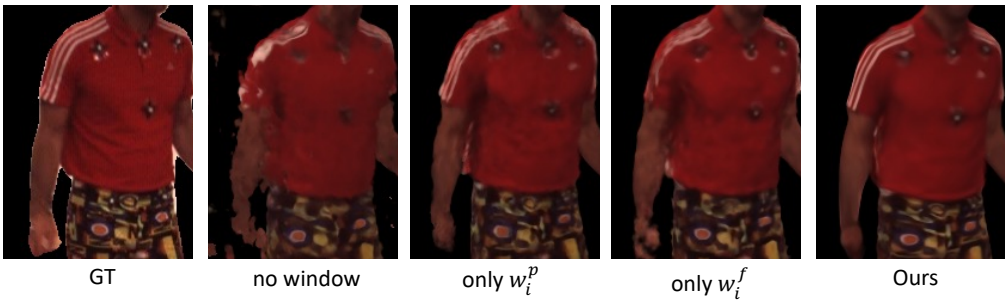

Figure 17: Ablation study on window functions with novel view synthesis.

Like ARAH Wang et al. (2022), we follow its settings and offer the geometry comparison results. Specifically, we also apply NeuS Wang et al. (2021) to obtain the pseudo geometry ground truth and compute quantitative metrics with L2 Chamfer Distance (CD). We show qualitative results in Fig. 14 and quantitative results in Tab. 5. Our method possesses better geometry reconstruction with smoother body surfaces than the template-free methods (HumanNeRF and MonoHuman) which introduce obvious floating artifacts in empty space. The geometry scores are slightly worse than Vid2Avatar which is a template based baseline and relies on SMPL parameters as a prior. The SDF-based surface rendering also helps Vid2Avatar achieve smoother shapes.

Complete Metrics on Human3.6M sequences. Besides the overall average numbers in the Tab. 2 of the main text, we also report a per-subject breakdown of the quantitative metrics against all baseline methods. Specifically, Tab. 7 lists the scores for the novel view synthesis while Tab. 8 details each method's results in novel pose rendering. Being consistent with the visual results shown in Fig. 5 and 6 of the main text, our method almost outperforms all baselines for all subjects.

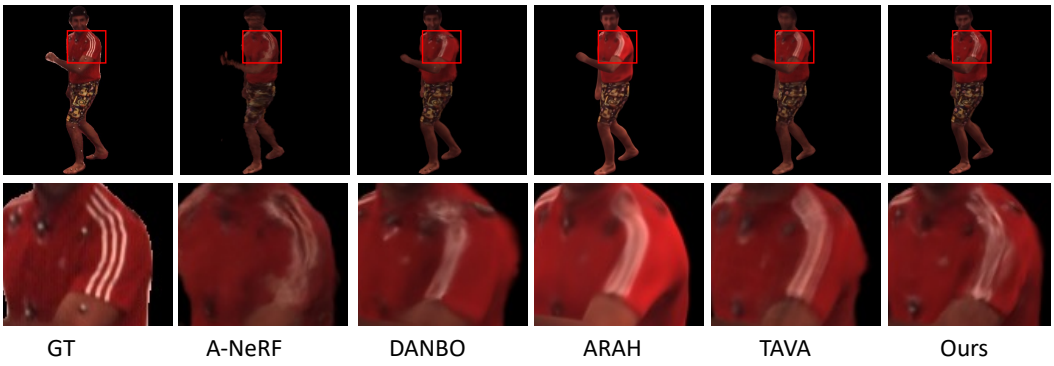

Figure 18: **Failure case.** How to generalize to challenging cases is still an open problem, where all methods fail to capture the stripe-wise textures under this pose.

Figure 19: **Additional comparison results with DANBO for novel view synthesis.** Due to the adaptive frequency modulation, our method can better synthesize the shape contour (e.g. hands on 1st column), the sharp patterns (e.g. the marker on 2nd column), and high-frequency details (e.g. the wrinkles on 1st column and the pant textures on 3rd column). Otherwise, DANBO which achieves frequency learning implicitly, blurs the sharp patterns and smoothes the fine-grained details.

Figure 20: **Additional comparison results with DANBO for novel pose rendering.** Due to the adaptive frequency modulation, our method successfully reduces the noisy artifacts on 1st column, reproduces the white markers on 2nd column and the black marker on 3rd column, reconstructs the sharp shape contours (e.g. the hand) on both 4th and 5th columns. Otherwise, DANBO which achieves frequency learning implicitly, blurs the sharp contours and smoothes the significant patterns with fine-grained details.

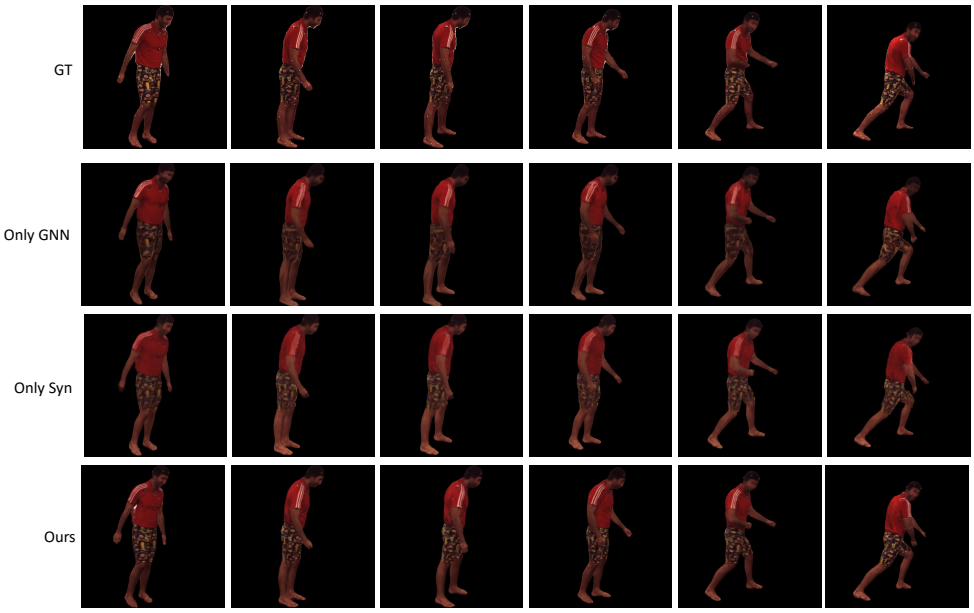

Figure 21: **Abaltion study on the network components with time consistency analysis.** Our full model can consistently produce more adaptive details (e.g. in the pant region), synthesize more structured textures (e.g. the stripes) and preserve more realistic contours (e.g. the leg shape). See texts for details.

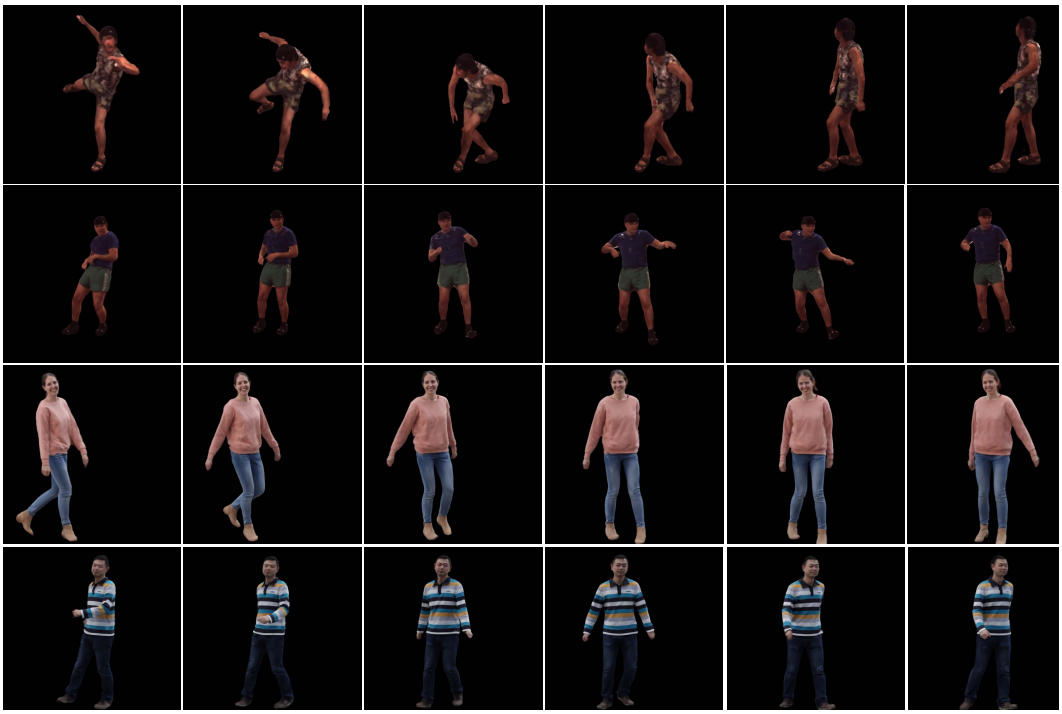

Figure 22: **Unseen pose renderings for the sequences** from both Human3.6M (top two rows) and MonoPerfCap (bottom two rows). Our network is robust to various poses across different datasets.

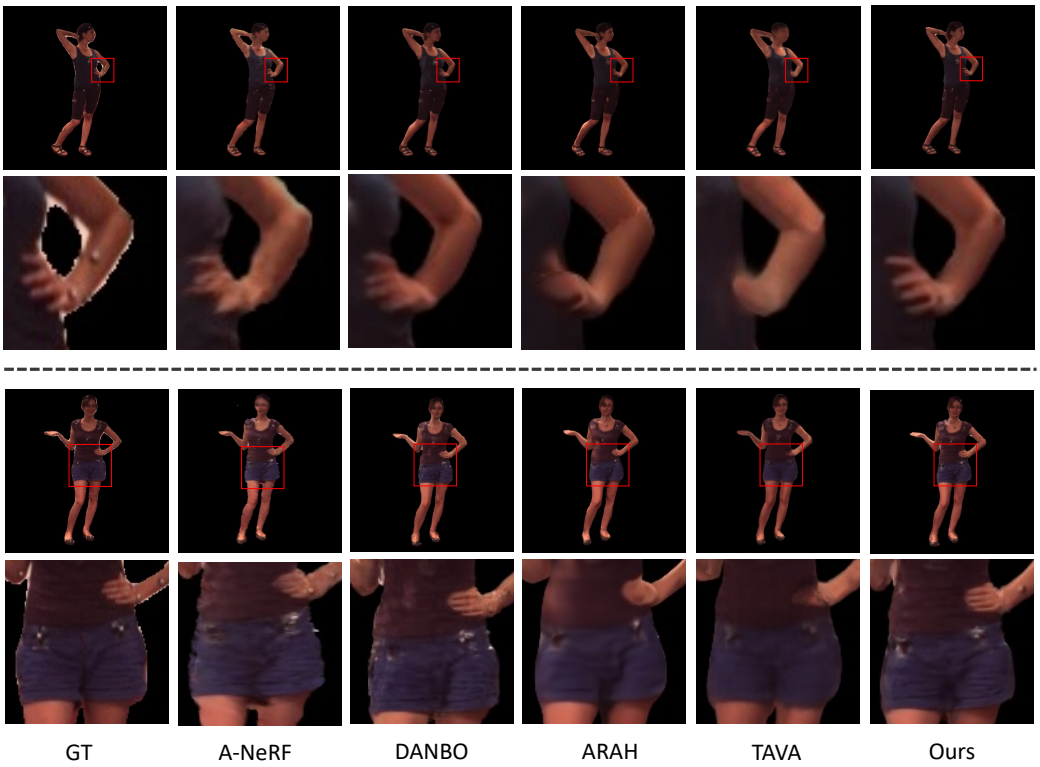

Figure 23: **Visual comparisons for novel view synthesis** (1st**row) and novel pose rendering** (2nd **row).** Compared to baselines, we can faithfully reconstruct the shape boundaries (e.g. the hands on both 1st and 2^{nd}rows) and the high-frequency details (e.g. the dynamic wrinkles on 2nd row).

Table 7: **Novel-view synthesis results on the Human3.6M Ionescu et al. (2011) test set.** Our method benefits from the explicit frequency modulations, leading to better perceptual quality. It matches or outperforms all baselines across subjects, reaching the best overall score in all three metrics.

	S1			S5			S6			S7			S8			S9			S11			Avg		
	PSNR↑	SSIM↑	LPIPS↓	PSNR	SSIM	LPIPS	PSNR	SSIM	LPIPS	PSNR	SSIM	LPIPS	PSNR↑	SSIM↑	LPIPS↓	PSNR	SSIM	LPIPS	PSNR	SSIM	LPIPS	PSNR	SSIM	LPIPS
Template/Scan-based prior																								
NeuralBody	22.88	0.897	0.139	24.61	0.917	0.128	22.83	0.888	0.155	23.17	0.915	0.132	21.72	0.894	0.151	24.29	0.911	0.122	23.70	0.896	0.168	23.36	0.905	0.140
Anim-NeRF	22.74	0.896	0.151	23.40	0.895	0.159	22.85	0.871	0.187	21.97	0.891	0.161	22.82	0.900	0.146	24.86	0.911	0.145	24.76	0.907	0.161	23.34	0.897	0.157
ARAH†	24.53	0.921	0.103	24.67	0.921	0.115	24.37	0.904	0.133	24.41	0.922	0.115	**24.15**	**0.924**	**0.104**	25.43	0.924	0.112	24.76	0.918	0.128	24.63	0.920	0.115
Template-free																								
A-NeRF	23.93	0.912	0.118	24.67	0.919	0.114	23.78	0.887	0.147	24.40	0.917	0.125	22.70	0.907	0.130	25.58	0.916	0.126	24.38	0.905	0.152	24.26	0.911	0.129
DANBO	23.95	0.915	0.107	24.85	0.923	0.107	24.54	0.903	0.129	24.45	0.920	0.113	23.36	0.917	0.116	26.15	0.925	0.108	25.58	0.917	0.127	24.69	0.917	0.116
TAVA	**25.28**	**0.928**	0.108	24.00	0.916	0.122	23.44	0.894	0.138	24.25	0.916	0.130	23.71	0.921	0.116	26.20	0.923	0.119	**26.17**	**0.928**	0.133	24.72	0.919	0.124
Ours	24.83	0.922	**0.102**	**24.97**	**0.925**	**0.102**	**24.55**	**0.903**	**0.124**	**24.65**	**0.923**	**0.107**	24.11	0.922	0.108	**26.39**	**0.929**	**0.100**	25.88	0.921	**0.128**	**25.06**	**0.921**	**0.110**

†: we evaluate using the officially released ARAH, which has undergone refactorization, resulting in slightly different numbers to the ones in Wang et al. (2022).

Table 8: **Novel pose rendering results on the Human3.6M Ionescu et al. (2011) test set.** Our pose guided frequency modulation pipeline generalizes better across unseen poses.

	S1			S5			S6			S7			S8			S9			S11			Avg		
	PSNR↑	SSIM↑	LPIPS↓	PSNR	SSIM	LPIPS	PSNR	SSIM	LPIPS	PSNR	SSIM	LPIPS	PSNR↑	SSIM↑	LPIPS↓	PSNR	SSIM	LPIPS	PSNR	SSIM	LPIPS	PSNR	SSIM	LPIPS
Template/Scan-based prior																								
NeuralBody	22.10	0.878	0.143	23.52	0.897	0.144	23.42	0.892	0.146	22.59	0.893	0.163	20.94	0.876	0.172	23.05	0.885	0.150	23.72	0.884	0.179	22.81	0.888	0.157
Anim-NeRF	21.37	0.868	0.167	22.29	0.875	0.171	22.59	0.884	0.159	22.22	0.878	0.183	21.78	0.882	0.162	23.73	0.886	0.157	23.92	0.889	0.176	22.61	0.881	0.170
ARAH†	23.18	0.903	0.116	22.91	0.894	0.133	23.91	0.901	0.125	22.72	0.896	0.143	22.50	0.899	0.128	24.15	0.896	0.135	23.93	0.899	0.143	23.27	0.897	0.134
Template-free																								
A-NeRF	22.67	0.883	0.159	22.96	0.888	0.155	22.77	0.869	0.170	22.80	0.880	0.182	21.95	0.886	0.170	24.16	0.889	0.164	23.40	0.880	0.190	23.02	0.883	0.171
DANBO	23.03	0.895	0.121	**23.66**	0.903	0.124	24.57	0.906	0.118	23.08	0.897	0.139	22.60	0.904	0.132	24.79	0.904	0.130	24.57	0.901	0.146	23.74	0.901	0.131
TAVA	**23.83**	**0.908**	0.120	22.89	0.898	0.135	24.54	0.906	0.122	22.33	0.882	0.163	22.50	0.906	0.130	24.80	0.901	0.138	**25.22**	**0.913**	0.145	23.52	0.899	0.141
Ours	23.73	0.903	**0.114**	23.65	**0.905**	**0.117**	**24.77**	**0.908**	**0.117**	**23.59**	**0.904**	**0.133**	**23.16**	**0.909**	**0.126**	**25.12**	**0.908**	**0.122**	25.03	0.907	**0.143**	**24.15**	**0.906**	**0.124**

†: we evaluate using the officially released ARAH, which has undergone refactorization, resulting in slightly different numbers to the ones in Wang et al. (2022).

Visual Comparisons with Baselines. Pose-modulated frequency learning plays a critical role in our method. To demonstrate the importance of this concept, we present more comparisons with DANBO which performs frequency modeling implicitly. In Fig. 19 and Fig. 20, our method is better at preserving large-scale shape contours as well as fine-grained textures with high-frequency details. Besides the results in Fig. 5 and 6 of the main text, we offer two more characters from Human3.6M sequences to evaluate the results on novel view synthesis and novel pose rendering. As shown in Fig. 23, we can successfully reproduce the detailed shape structures (e.g. the hand on 1st row) and high-frequency wrinkles (e.g. 2nd row). These findings stay consistent with the discussions in main text and the quantitative results in Tab. 7-8.

Ablation studies. We formulate our framework from connections between frequencies and pose contexts. To more comprehensively evaluate the effectiveness of our pose-guided frequency modulation concept, we provide one more visual comparison in Fig. 16. It is clear that only our full model successfully synthesizes high frequency patterns, e.g., shown in the pant region.

To additionally showcase the capabilities in reproducing the frequency distributions, we illustrate the frequency histograms for the ground truth images and the network outputs in Fig. 12. Our full model remarkably reduces the gap to the ground truth histograms qualitatively and quantitatively.

Moreover, as shown in Fig. 21, our full model presents much better time consistency than ablated models. Specifically, the full model constantly preserves more adaptive details (e.g. the patterns in the pant region) than the $\mathrm{onlyGNN}$ model and synthesizes more structured stripe-wise patterns than the $\mathrm{onlySyn}$ model. Moreover, the $\mathrm{onlySyn}$ model distorts the leg shape on the last column.

To highlight the empirical importance of the window function w_i^p and w_i^f, Fig. 17 depicts qualitative differences between the ablated baselines and our full model. It is clear that using w_i^p or w_i^f alone cannot produce the image quality of the full model, demonstrating the necessity of the window function design. Tab. 6 additionally presents the quantitative comparisons for all ablation models, further supporting the aforementioned discussions.

Geometry Visualization. The attached video visualizes two examples for the geometry reconstruction comparison with DANBO. Like the discussions in the main text, we can present overall more complete body outline and a smoother surface than the baseline. Please see video for details.

Motion Retargeting. Generality to unseen human poses is critical to a number of down-streamed applications, e.g. Virtual Reality. We provide two examples in the attached video. Although our

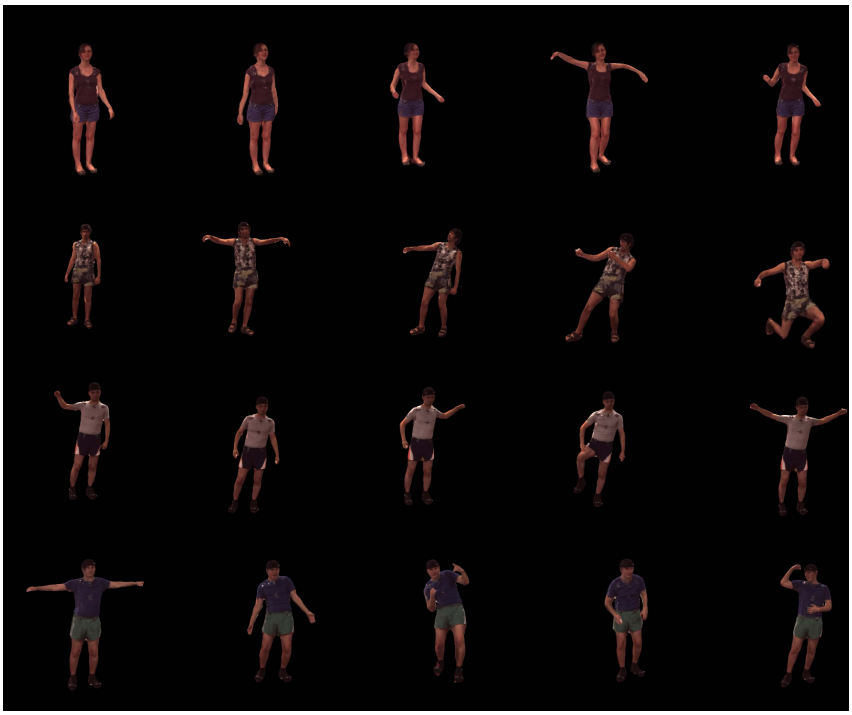

Figure 24: Additional visual results for novel view synthesis. It is clear that our method can faithfully reproduce a larger spectrum of details, from large-scale shape contours (e.g. 1st row) to fine-grained textures (e.g. 2nd row), across different scenes.

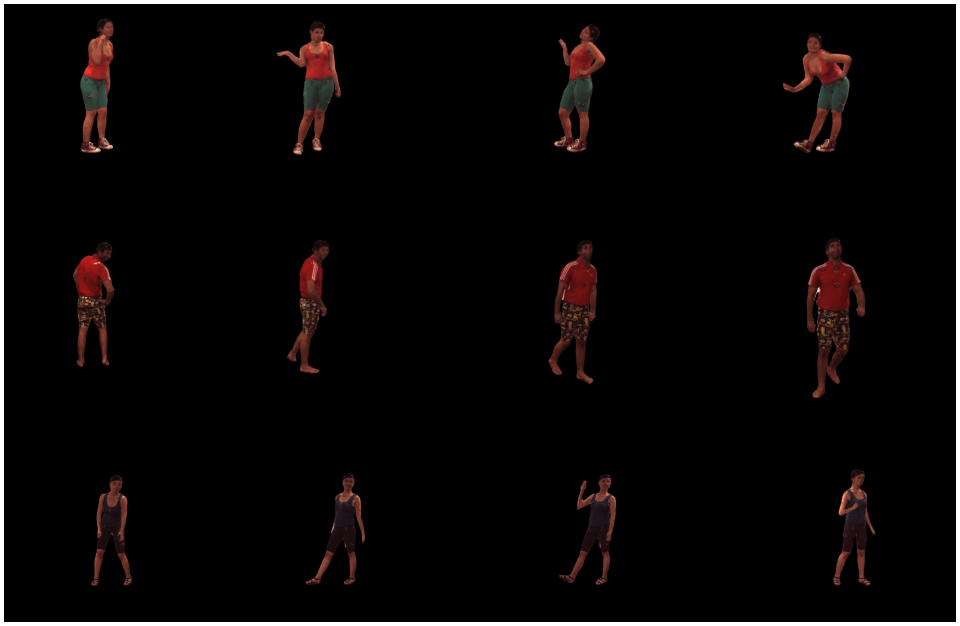

Figure 25: Additional visual results for novel pose rendering. It is clear that our method can generalize well to the unseen poses with different patterns.

model is trained on the Human3.6M sequences, it can consistently be adapted to the unseen poses with challenging movements. The desired time consistency convincingly demonstrates our strong generality to out-of-the-distribution poses.

More Visual Results. In order to assess the performance of our method in handling unseen camera views and human skeletons, we provide additional results showcasing novel view synthesis in Fig. 24 and novel pose rendering in Fig. 25. We also illustrate the rendering results for different sequences of Human3.6M and MonoPerfCap datasets for unseen poses in Fig. 22.

From the results, it is evident that our method, with its developed frequency modulation modeling, effectively captures diverse texture details and shape contours even when confronted with human poses that differ significantly from those in the training set. This empirical advantage can be attributed to the adaptive detail modeling capabilities facilitated by pose-modulated frequency learning strategy.

D Limitations and Discussions

Although our method is faster than other neural field approaches, computation time remains a constraint for real-time use. Our method is also person-specific, demanding individual training for each person. And our method heavily relies on accurate camera parameters and lacks support for property editing like pattern transfer. Thus this approach shines with ample training time and available data. Additionally, as shown in Fig. 18, under extreme challenges, our method cannot vividly reproduce the desired patterns but introduces blurry artifacts. However, we would like to note that, how to advance the generalization to such cases is still open since the existing methods suffer from similar or worse artefacts as well.

Social Impacts. Our research holds the promise of greatly improving the efficiency of human avatar modeling pipelines, promoting inclusivity for underrepresented individuals and activities in supervised datasets. However, it's imperative to address the ethical aspects and potential risks of creating 3D models without consent. Users must rely on datasets specifically collected for motion capture algorithm development, respecting proper consent and ethical considerations. Furthermore, in the final version, all identifiable faces will be blurred for anonymity.